Edinburgh Research Explorer

Adaptive Total Lagrangian Eulerian SPH for high-velocity impacts

OPEN ACCESS

Journal Pre-proof

Adaptive Total Lagrangian Eulerian SPH for high-velocity impacts

J. Young, F. Teixeira-Dias, A. Azevedo, F. Mill

Please cite this article as: J. Young, F. Teixeira-Dias, A. Azevedo, F. Mill, Adaptive Total Lagrangian Eulerian SPH for high-velocity impacts, *International Journal of Mechanical Sciences* (2020), doi: https://doi.org/10.1016/j.ijmecsci.2020.106108

This is a PDF file of an article that has undergone enhancements after acceptance, such as the addition of a cover page and metadata, and formatting for readability, but it is not yet the definitive version of record. This version will undergo additional copyediting, typesetting and review before it is published in its final form, but we are providing this version to give early visibility of the article. Please note that, during the production process, errors may be discovered which could affect the content, and all legal disclaimers that apply to the journal pertain.

Adaptive Total Lagrangian Eulerian SPH for high-velocity impacts
J. Young, F. Teixeira-Dias, F. Mill

Highlights

- *A novel SPH formulation is presented for high-velocity impact problems.*

- *Particle kernels adaptively convert from a Total Lagrangian to an Eulerian formulation.*

- *Mixed kernel-and-gradient correction is used to improve consistency.*

- *A novel form of artificial viscosity is presented for the Total Lagrangian formulation.*

- *The adaptive coupled formulation is shown to outperform either formulation independently.*

Total Lagrangian particles

● = ○

● = ✕

Adaptively converted
Eulerian particles

High-velocity impact of a circular
projectile on a rectangular target

Eulerian interface
neighbours

Interface

Total Lagrangian
interface neighbours

δx

Eulerian particles

Total Lagrangian particles

Particle Conversion

Once damaged, Total Lagrangian
particles and their neighbours,
convert to Eulerian particles.
Fracture is handled naturally.

b a

κh

b a

κh

● Total Lagrangian Particle
● Damaged Total Lagrangian Particle

✕ Eulerian Particle
✕ Damaged Eulerian Particle

Adaptive Total Lagrangian Eulerian SPH for high-velocity impacts

J. Young[a], F. Teixeira-Dias[a,*], A. Azevedo[b], F. Mill[a]

[a]*School of Engineering, The University of Edinburgh, Edinburgh EH9 3FG, UK*
[b]*Department of Weapon Systems & Ballistics, Royal Military Academy, Brussels, Belgium*

Abstract

This paper presents a novel coupling between the Total Lagrangian and Eulerian formulations of the Smooth Particle Hydrodynamics (SPH) method. It is implemented such that a Total Lagrangian formulation can adaptively convert to an Eulerian formulation (referred to as AdapTLE in this work) and applied to high-velocity impact problems. The novel coupling makes use of the mixed kernel-and-gradient correction scheme, which is applied in order to improve consistency and conserve momentum. Additionally, the symmetrical terms, which are often found in SPH, are included in the derivation of the conservation equations to reduce the number of calculations required. A novel implementation of artificial viscosity is suggested for the Total Lagrangian formulation, which makes use of the kernel gradient in the undeformed state and therefore does not require neighbour lists to be updated. This form of artificial viscosity can be applied to a singularly Total Lagrangian formulation or a coupled one. Numerical examples including a patch test, and two-dimensional and three-dimensional high-velocity impact problems were simulated to evaluate this novel coupling method and demonstrate the benefits of AdapTLE, which was found to produce superior results to either a Total Lagrangian or Eulerian formulation independently. This was due to the retention of a Total Lagrangian formulation until severe distortions required the conversion to an Eulerian formulation, which significantly reduced the effect of the tensile instability in the latter.

Keywords: Smooth Particle Hydrodynamics, SPH, Corrected SPH, Eulerian, Total Lagrangian, Coupled, Solids, High-velocity impact

*Corresponding author: f.teixeira-dias@ed.ac.uk

1. Introduction

Smooth Particle Hydrodynamics (SPH) was first formulated for astrophysical problems by Gingold and Monaghan [1] in 1977 and by Lucy [2] later that year. It is a meshless particle method whereby the governing equations are discretised and calculated based on the physical properties at particle locations. As detailed by Liu and Liu [3], SPH has been extended to encompass a broad range of applications in both fluid and solid mechanics. These vary from coastal hydrodynamics, to magneto-hydrodynamics to explosive detonations. SPH wasn't applied to solid mechanics until 1991 when Libersky and Petschek [4] modelled a plane-strain Taylor impact test. Subsequently, a numerical instability in the method, referred to as "tensile instability", was investigated by Swegle et al. [5] where particles were observed to clump together. They attributed the tensile instability to a combination of the sign of the kernel's second derivative and negative pressure. Following the analysis carried out by Swegle et al. a number of attempts have been made to address tensile instability. Dyka and Ingel [6] introduced the concept of stress points to SPH whereby kinematic information is carried by one set of particles and another set carries stress information. Monaghan [7], shortly followed by Gray et al. [8], introduced artificial stress, which adds an additional stress term to the conservation of momentum equation. In the development by Gray et al. the repulsive stress term is only added to particles which have a positive principal stress.

Bonet et al. [9], Belytschko et al. [10] and Rabczuk et al. [11] are referred to for the descriptions of the formulations used. According to Belytschko et al. [10], "*formulations in terms of the Lagrangian measures of stress and strain in which derivatives and integrals are taken with respect to the Lagrangian (material) coordinates X* [are] *called total Lagrangian formulations*". These authors continue to state that "*formulations expressed in terms of Eulerian measures of stress and strain in which derivatives and integrals are taken with respect to the Eulerian (spatial) coordinates x* [are] *often called updated Lagrangian formulations*". The common convention to refer to the second of these formulations as an Eulerian formulation is followed [9, 12]. Consequently, in this work any reference to Total Lagrangian or Eulerian kernels refers to kernels that are calculated in the material and spatial coordinates, respectively [11]. Additionally, Total Lagrangian and Eulerian particles are particles that make use of a kernel in either the material or spatial coordi-

4

nates, respectively. The term "mixed kernel-and-gradient" correction is used in the following and is written as a shortened version of the first-order mixed kernel-and-gradient consistency correction developed by Bonet and Lok [13]. The hyphenation in the full terminology is borrowed from Basa et al. [14] as it makes it transparent that "mixed kernel-and-gradient" correction refers to a specific type of correction.

Tensile instability was completely circumvented by Belytschko et al. [15] who noted that it was a product of using an Eulerian kernel, this being the weighting function in the current configuration. Belytschko et al. showed that tensile instability does not manifest when the kernel is a function of the material or Lagrangian co-ordinates, which is known as a Total Lagrangian [10] formulation. They further showed that another instability caused by rank deficiency and known as "zero-energy" modes can occur in either Eulerian or Total Lagrangian kernel form. Despite not suffering tensile instability, the Total Lagrangian formulation does have limitations. As the initial configuration of particles is used as the reference condition, the Total Lagrangian formulation may become unstable in the presence of large distortions. An obvious solution might be to update the reference condition, but as discussed by Vidal et al. [16], this may activate zero-energy modes and require additional stabilisation terms.

In the Eulerian formulation of the SPH method there are generally two ways to evaluate density. Liu and Liu [17] refer to these as the summation density and the continuity density methods. Similarly, numerous approaches have been proposed to calculate the internal forces between particles. It was Bonnet and Lok [13] who gave the variationally consistent forms of the momentum equations and highlighted that they must be used with the correct density equation, as was further confirmed by Price [18]. They also derived the conditions that must be satisfied in order to conserve linear and angular momentum, mentioning, and later showing, that conventional SPH generally does not conserve angular momentum. This phenomenon was further investigated by Hoover et al. [19] who attempted to remedy the problem by applying strong XSPH, which is a technique whereby the velocity used to update a particle's position is in part interpolated from its neighbours [20]. Having stated the requirements for the conservation of angular momentum, Bonet and Lok derive a mixed kernel and gradient correction technique or "mixed correction". This mixed correction is a combination of gradient correction, which modifies the gradient of the

5

kernel, and kernel correction, which alters the kernel itself. Gradient correction guarantees the conservation of angular momentum and that the gradient of a linear field will be exactly calculated given that the internal forces are variationally consistent with the density equation. These authors use a simplified version of the kernel correction originally proposed by Liu et al. [21] and Li and Liu [22]. This is often known as kernel normalisation or the Shepard function and restores 0th order consistency [3]. Having written their form of mixed kernel-and-gradient correction, Bonet and Lok dispense with the symmetrical term used in the velocity gradient as it is no longer required to ensure that the velocity divergence vanishes for a constant field. Symmetrical terms are commonly used in SPH and are discussed in more detail by Vignjevic et al. [23].

Both the Eulerian and Total Lagrangian formulations of SPH have their own strengths and weaknesses. Simulations involving impact and fracture would benefit from a coupled approach whereby the appropriate parts of the domain could take advantage of the computational efficiency and stability of the Total Lagrangian formulation and the ability to model large distortions of the Eulerian formulation. Little work has been done on coupling the Eulerian and Total Lagrangian formulations of SPH other than by Lacome et al. [24]. They developed a model where particles with Eulerian kernels treat all other particles as having Eulerian kernels. The same treatment is carried out by particles with Total Lagrangian kernels. The methodology proposed in this work differs as modification is only required for particles with support domains which include particles of a differing kernel type. Furthermore, in this paper, particle kernel type conversion and the application of mixed kernel-and-gradient correction, artificial viscosity and artificial stress to a coupled formulation is described.

When coupling the two formulations, the overlaps between the two kernel types require special treatment. Consider an Eulerian particle in whose influence range there are only other Eulerian particles. In this case, no modification is required to the formulation and the for Eulerian SPH is followed. The same applies to a Total Lagrangian particle in whose influence range there are only other Total Lagrangian particles. However, modifications are required in the scenario where an Eulerian particle has a Total Lagrangian particle in its support domain and vice versa. In this work, such a region is referred to as the interface zone. Figure 1 displays an example of a discretised continuum with this zone highlighted.
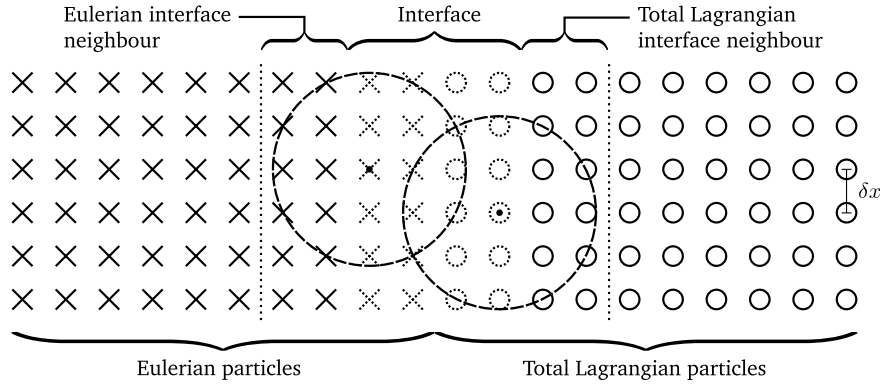
6

Figure 1: Representative continuum discretised into Total Lagrangian and Eulerian particles with noteworthy zones highlighted. The particle influence range is approximately equal to $2\delta x$ for illustrative purposes.

The numerical implementation applied in this work is explained in three sections. Firstly, the conservation equations are given for both the Eulerian and Total Lagrangian formulations. These equations include the effect of mixed kernel-and-gradient correction and the contributions from artificial stress and artificial viscosity. Next, the AdapTLE coupling methodology and particle conversion strategy is explained. Lastly, the use of a contact algorithm is described. In order to validate the proposed model three numerical examples are given. The first example demonstrates how the artificial stress can be integrated into the coupled formulation and how fields can smoothly transition between at the interface between particle kernel types. The final two numerical examples, show how the AdapTLE approach, where the particle kernel type can switch from an Eulerian formulation to a Total Lagrangian formulation, is better suited to high-velocity impact problems than either formulation independently.

7

2. Numerical implementation

2.1. Conservation Equations

The spatial equations used to describe the evolution of mass, momentum and energy are given by [25]

$$
\begin{aligned}
\frac{\mathrm{d}\rho_a}{\mathrm{d}t} &= -\rho_a \sum_{b \in \mathbb{N}_{(a)}} V_b (\mathbf{v}_b - \mathbf{v}_a) \cdot \widetilde{\nabla}_a \widetilde{W}_{ab} \\
\frac{\mathrm{d}\mathbf{v}_a}{\mathrm{d}t} &= -\frac{1}{m_a} \sum_{b=1} V_a V_b (\boldsymbol{\sigma}_b \widetilde{\nabla}_b \widetilde{W}_{ba} - \boldsymbol{\sigma}_a \widetilde{\nabla}_a \widetilde{W}_{ab}) \\
\frac{\mathrm{d}e_a}{\mathrm{d}t} &= \sum_{b=1} V_a V_b (\mathbf{v}_b - \mathbf{v}_a) \cdot \boldsymbol{\sigma}_a \widetilde{\nabla}_a \widetilde{W}_{ab} \\
\left(\frac{\mathrm{d}\mathbf{v}_a}{\mathrm{d}t}\right)_{\mathrm{diss}} &= \sum_{b=1}^{N} \frac{m_b \Pi_{ab}}{2} \left(\widetilde{\nabla}_b \widetilde{W}_{ba} - \widetilde{\nabla}_a \widetilde{W}_{ab}\right) \\
\left(\frac{\mathrm{d}e_a}{\mathrm{d}t}\right)_{\mathrm{diss}} &= \sum_{b=1}^{N} \frac{m_a m_b \Pi_{ab}}{4} (\mathbf{v}_b - \mathbf{v}_a) \cdot \left(\widetilde{\nabla}_b \widetilde{W}_{ba} - \widetilde{\nabla}_a \widetilde{W}_{ab}\right) \\
\left(\frac{\mathrm{d}\mathbf{v}_a}{\mathrm{d}t}\right)_{\mathrm{stress}} &= -\sum_{b=1}^{N} \frac{m_b f_{ab}^{n_{\mathrm{as}}}}{2} \left(\mathbf{R}_b \widetilde{\nabla}_b \widetilde{W}_{ba} - \mathbf{R}_a \widetilde{\nabla}_a \widetilde{W}_{ab}\right) \\
\left(\frac{\mathrm{d}e_a}{\mathrm{d}t}\right)_{\mathrm{stress}} &= -\sum_{b=1}^{N} \frac{m_a m_b f_{ab}^{n_{\mathrm{as}}}}{2} (\mathbf{v}_b - \mathbf{v}_a) \cdot \left(\mathbf{R}_b \widetilde{\nabla}_b \widetilde{W}_{ba} - \mathbf{R}_a \widetilde{\nabla}_a \widetilde{W}_{ab}\right)
\end{aligned}
\tag{1}
$$

and the material equations by [25]

$$
\begin{aligned}
\rho_a &= \frac{\rho_{a,0}}{\det\left[\left(\sum_{b=1} V_{b,0}(\mathbf{u}_b - \mathbf{u}_a) \otimes \widetilde{\nabla}_{a,0} \widetilde{W}_{ab,0}\right) + \mathbf{I}\right]} \\
\frac{\partial \mathbf{v}_a}{\partial t} &= -\frac{1}{m_a} \sum_{b=1} V_{a,0} V_{b,0} \left(\mathbf{P}_b \widetilde{\nabla}_{b,0} \widetilde{W}_{ba} - \mathbf{P}_a \widetilde{\nabla}_{a,0} \widetilde{W}_{ab}\right) \\
\frac{\partial e_a}{\partial t} &= \sum_{b=1} V_{a,0} V_{b,0} (\mathbf{v}_b - \mathbf{v}_a) \cdot \mathbf{P}_a \widetilde{\nabla}_{a,0} \widetilde{W}_{ab,0} \\
\left(\frac{\partial \mathbf{v}_a}{\partial t}\right)_{\mathrm{diss}} &= \sum_{b=1}^{N} \frac{m_b \Pi_{ab}}{2} \left(J_a^{-1} \mathbf{F}_b^{-\mathsf{T}} \widetilde{\nabla}_{b,0} \widetilde{W}_{ba} - J_b^{-1} \mathbf{F}_a^{-\mathsf{T}} \widetilde{\nabla}_{a,0} \widetilde{W}_{ab}\right) \\
\left(\frac{\partial e_a}{\partial t}\right)_{\mathrm{diss}} &= \sum_{b=1}^{N} \frac{m_a m_b \Pi_{ab}}{4} (\mathbf{v}_b - \mathbf{v}_a) \cdot \left(J_a^{-1} \mathbf{F}_b^{-\mathsf{T}} \widetilde{\nabla}_{b,0} \widetilde{W}_{ba} - J_b^{-1} \mathbf{F}_a^{-\mathsf{T}} \widetilde{\nabla}_{a,0} \widetilde{W}_{ab}\right)
\end{aligned}
\tag{2}
$$

where the subscripts a and b describe a particle and its neighbour, ρ is density, V is volume, m is mass, e is energy (not energy per unit mass), t is time, J is the Jacobian, Π is an artificial viscosity

scalar, f and n_{as} are an artificial stress scalar and constant, $\mathbf{v}$ is velocity, $\mathbf{u}$ is displacement, $\mathbf{I}$ is the identity matrix, σ is the Cauchy sheer stress, $\mathbf{P}$ is the first Piola-Kirchhoff stress, $\mathbf{F}$ is the deformation matrix, $\mathbf{R}$ is an artificial stress tensor, $\widetilde{\nabla}_a \widetilde{W}_{ab}$ is the spatial description of the corrected gradient of the corrected kernel and, $\widetilde{\nabla}_{a,0} \widetilde{W}_{ab,0}$ is the material description. It is noted that

$$\widetilde{\nabla}_a \widetilde{W}_{ab} = \mathbf{K}_a \nabla_a \widetilde{W}_{ab} \tag{3}$$

where the gradient of the corrected kernel is calculated by

$$\nabla_a \widetilde{W}_{ab} = \frac{\nabla_a W_{ab} \left(\sum_{b=1}^{N} V_b W_{ab} \right) - \left(\sum_{b=1}^{N} V_b \nabla_a W_{ab} \right) W_{ab}}{\left(\sum_{b=1}^{N} V_b W_{ab} \right)^2} \tag{4}$$

The correction matrix $\mathbf{K}$ can then be defined using the gradient of the corrected kernel as

$$\mathbf{K}_a = \left[\sum_{b=1}^{N} V_b \nabla_a \widetilde{W}_{ab} \otimes (\mathbf{x}_b - \mathbf{x}_a) \right]^{-1} \tag{5}$$

Note that for the material equations, $\widetilde{\nabla}_{a,0} \widetilde{W}_{ab}$ is calculated once, in the reference configuration and then held constant, whilst in the spatial equations, $\widetilde{\nabla}_a \widetilde{W}_{ab}$ is calculated at every time step. Mixed kernel-and-gradient correction is implemented as it combines the benefits of both: the 0th order consistency of kernel approximations using the kernel correction and the 1st order consistency of the kernel gradient approximations, along with the conservation of angular momentum, using the kernel gradient correction.

The dissipative terms calculate the impact of artificial viscosity, where Monaghan [26, 27] gives the following commonly used form:

$$\Pi_{ab} = \begin{cases} \dfrac{-\alpha \bar{c}_{ab} \mu_{ab} + \beta \mu_{ab}^2}{\bar{\rho}_{ab}} & \text{if } (\mathbf{v}_a - \mathbf{v}_b) \cdot (\mathbf{x}_a - \mathbf{x}_b) < 0 \\ 0 & \text{if } (\mathbf{v}_a - \mathbf{v}_b) \cdot (\mathbf{x}_a - \mathbf{x}_b) \geq 0 \end{cases} \tag{6}$$

and

$$\mu_{ab} = \frac{h(\mathbf{v}_a - \mathbf{v}_b) \cdot (\mathbf{x}_a - \mathbf{x}_b)}{|(\mathbf{x}_a - \mathbf{x}_b)|^2 + 0.01 h^2} \tag{7}$$

The barred notation over c and ρ denotes an average value between particles a and b. The speed of sound is denoted by c and the constant α is dominant for small velocity differences and produces

9

a bulk viscosity [17, 18]. The β term is similar to the von Neumann-Richtmyer artificial viscosity and becomes dominant for large velocity differences [18]. The 0.01 in the denominator is used to prevent singularities. The equations for $d\mathbf{v}_a/dt$ and $(d\mathbf{v}_a/dt)_{\text{diss}}$ differ slightly in the spatial equations (and in their material counterparts), as the units for Π_{ab} are that of p/ρ^2, where p is pressure. The dissipative term in the material equations 2 was found by equating the spatial and material momentum equations and uncovering the equivalence that

$$\boldsymbol{\sigma}_b \widetilde{\nabla}_b \widetilde{W}_{ba} - \boldsymbol{\sigma}_a \widetilde{\nabla}_a \widetilde{W}_{ab} = J_a^{-1} \boldsymbol{\sigma}_b \mathbf{F}_b^{-\mathsf{T}} \widetilde{\nabla}_{b,0} \widetilde{W}_{ba} - J_b^{-1} \boldsymbol{\sigma}_a \mathbf{F}_a^{-\mathsf{T}} \widetilde{\nabla}_{a,0} \widetilde{W}_{ab} \ , \tag{8}$$

whilst noting that for artificial viscosity, the stress term $\boldsymbol{\sigma}_a = \boldsymbol{\sigma}_b = \Pi_{ab}\mathbf{I}$, such that

$$\Pi_{ab}\mathbf{I}\left(\widetilde{\nabla}_b \widetilde{W}_{ba} - \widetilde{\nabla}_a \widetilde{W}_{ab}\right) = \Pi_{ab}\mathbf{I}\left(J_a^{-1}\mathbf{F}_b^{-\mathsf{T}}\widetilde{\nabla}_{b,0}\widetilde{W}_{ba} - J_b^{-1}\mathbf{F}_a^{-\mathsf{T}}\widetilde{\nabla}_{a,0}\widetilde{W}_{ab}\right) \ . \tag{9}$$

The above is used to transform artificial viscosity into the reference coordinates, such that the spatial corrected gradient of the corrected kernel is not required for the Total Lagrangian formulation. The effect of this transformation is that particles with Total Lagangian kernels can now make use of artificial viscosity without requiring an update to their neighbour lists, this being one of the most computationally intense components of the SPH method. This is not only beneficial in a simulation that only makes use of Total Lagrangian kernels but is similarly useful in simulations that make use of an adaptive kernel conversion.

The artificial stress terms can be used in two-dimensional problems. The term f_{ab} is

$$f_{ab} = \frac{W_{ab}}{W(\Delta p)} \tag{10}$$

where Δp is the average particle spacing. The previously mentioned scalar n_{as} is a factor that controls the magnitude of the artificial stress [7]. The artificial stress tensor is

$$\mathbf{R}_{ab} = (\mathbf{R}_a + \mathbf{R}_b) \tag{11}$$

where Gray el al. [8] calculate $\mathbf{R}_a$ and $\mathbf{R}_b$ by modifying the principal components of the Cauchy stress tensor, which are tensile, by a constant ($\epsilon_{as} = 0.3$), and then rotating the resulting tensor back to its original coordinates.

Symmetrical terms are included in equation sets 1 and 2 such that the contribution from $b = a = 0$, resulting in a model that is more computationally efficient and conceptually simple.

10

2.2. AdapTLE Coupling Methodology

The spatial and material equations given, do not describe how to accommodate neighbouring particles of differing kernel type, i.e particles which are in the interface zone. It is trivial to transform a material stress into its spatial stress through

$$\boldsymbol{\sigma} = J^{-1}\mathbf{F}\mathbf{P}^{\mathsf{T}} \tag{12}$$

It is more complex, however, to do the opposite as is needed for the Total Lagrangian conservation of momentum equation. This equation requires that the neighbouring Eulerian particles have a first Piola-Kirchhoff stress tensor. The calculation of this stress tensor requires a deformation gradient. Therefore, the Eulerian particles in the interface zone must calculate their deformation gradient in the reference configuration as

$$\mathbf{F}_a = \left[\sum_{b=1}^{N} V_{b,0}(\mathbf{u}_b - \mathbf{u}_a) \otimes \overline{\nabla}_{a,0} \widetilde{W}_{ab,0} \right] + \mathbf{I} \tag{13}$$

Lacome et al. [24] calculated the deformation gradient for all particles whilst the coupling method described here only extends the range of the Total Lagrangian kernel type to the neighbours of the Eulerian interface particles. Consequently, it requires that these Eulerian interface neighbours do not experience any large distortions or else the deformation gradient of the Eulerian interface particles will become nonphysical. Using this method the internal forces are not coupled (i.e. summations are over one kernel type, not a mixture) and as a result it is compatible with artificial stress. Note that in this method, the Eulerian particles must search through the Total Lagrangian particles for neighbours at every time step, while the Total Lagrangian particles only search for Eulerian neighbours in the undeformed configuration. Therefore, the list of interface neighbours can differ in the material and spatial coordinates.

The application of the mixed kernel-and-gradient correction to this coupling method requires further explanation. Namely how the interface particles, which make use of Total Lagrangian kernels, are required to find their nearest neighbours in the spatial coordinates. This can be highlighted by inspecting the gradient of the corrected kernel

$$\nabla_a \widetilde{W}_{ab} = \frac{\nabla_a W_{ab} \left(\sum_{b=1}^{N} V_b W_{ab} \right) - \left(\sum_{b=1}^{N} V_b \nabla_a W_{ab} \right) W_{ab}}{\left(\sum_{b=1}^{N} V_b W_{ab} \right)^2} \tag{14}$$

11

and noticing that the summations $\sum_{b=1}^{N} V_b W_{ab}$ and $\sum_{b=1}^{N} V_b \nabla_a W_{ab}$ must be calculated for particles in the interface zone that use Total Lagrangian kernels. This is required for the corrected gradient of the corrected kernel $\widetilde{\nabla}_b \widetilde{W}_{ba}$ in the spatial conservation of momentum equation. Therefore, the mixed kernel-and-gradient correction extends the range of the Eulerian kernel type to the neighbours of the Total Lagrangian interface particles (see Figure 1).

2.3. AdapTLE Particle Kernel Conversion

The conversion from the Total Lagrangian kernel type to the Eulerian kernel type is theoretically trivial. Once converted to an Eulerian kernel, a particle swaps from the Total Lagrangian conservation equations (equations 2) to the Eulerian conservation equations (equations 1). It is assumed that it is only desirable for a particle to convert kernel type if it has reached some deformation or damage criteria. According to de Vuyst and Vignjevic [28], who modelled fracture using the Total Lagrangian method, "*it is not sufficient to simply set the stress of a failed particle to zero and to remove it from the neighbour lists*". These authors explain that a particle may have a support domain that encompasses both fractured particles and additional particles on the other side of the fracture line. They state that, in this case, the stress state becomes non-physical. An example of this is displayed in the left hand-side image in Figure 2.
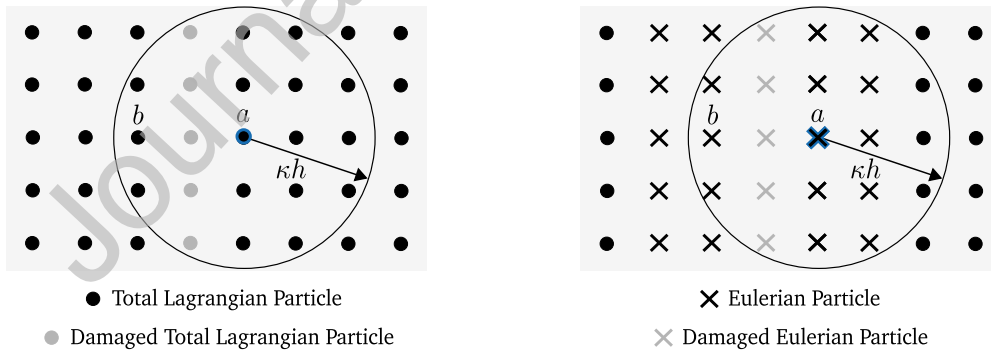

● Total Lagrangian Particle ✕ Eulerian Particle

● Damaged Total Lagrangian Particle ✕ Damaged Eulerian Particle

Figure 2: The left hand-side image highlights how a particle *a* can be influenced by another particle *b* across a fracture path due to the range of the support domain. If using a Total Lagrangian kernel, particles *a* and *b* will continue to influence each other unless the reference configuration is updated. The right hand-side image displays damaged particles and their neighbours converting kernel types. Once displaced, the support domains will no longer overlap.

In this image particles *a* and *b* are located on either side of damaged particles. Regardless,

particle *a* uses particle *b* within its summations and will continue to do so as these particles were neighbours in the reference configuration. In order to prevent particles interpolating across fracture lines, or the creation of non-physical deformation gradients, once a particle fractures it converts kernel type along with its neighbours. This is highlighted by the right hand-side image in Figure 2. Using this approach, the Eulerian particles will separate until the support domains no longer overlap. A further benefit to this approach is that no particles need to be removed from neighbour lists or have their field variables set to zero.

2.4. Contact algorithm

The frictionless contact algorithm developed by Vignjevic et al. [29, 30] is used as it can be implemented with both the Eulerian and Total Lagrangian formulations and does not produce artificial shear or friction. Vignjevic et al. derive a contact force given by

$$\left(\frac{d\mathbf{v}_a}{dt}\right)_{\text{cont}} = -\frac{1}{m_a}\sum_{b=1}^{N_{\text{cont}}} V_a V_b K_{\text{ca}} n_{\text{ca}} \frac{W_{ab}^{n_{\text{ca}}-1}}{W(\Delta p)^{n_{\text{ca}}}} \nabla_a W_{ab} \tag{15}$$

Summations only take place between particles in separate bodies. In this equation K_{ca} is a contact stiffness penalty parameter, Δp is the average particle spacing and n_{ca} is an exponent of the kernel values and a multiplier. This contact algorithm also conserves both momentum and energy. It is presumed that this algorithm is termed 'frictionless' as the resulting force acts along the straight line connecting particles. As a result, the shear stresses that are generated if using the conservation equations to simulate contact do not manifest and cause friction. Unlike the artificial viscosity equation, this algorithm has not been modified for a Total Lagrangian or a mixed kernel-and-gradient correction formulation. Therefore, the contact particles will require kernel and kernel gradient values in the deformed state. This does not introduce an inconsistency with the conservation equations which use mixed kernel-and-gradient correction (equation sets 1 and 2) as the contact algorithm is solely used to transfer momentum between two bodies. This could be achieved by using a force defined by the Lennard-Jones potential, which makes no use of the kernel or kernel gradient values. If using kernel values it is simple to define a function that increases as the separation between particles decreases, regardless of the discretisation resolution. Additionally, the kernel values automatically ensure that the force acts along the straight-line connecting

13

particles. Furthermore, applying mixed kernel-and-gradient correction to the contact potential equation would result in a contact potential force which was not equal and opposite between particle pairs and this would damage the conservation properties of the formulation.

In order to ensure the conservation of energy, the contact force must also be added to the evolution of internal energy. The contribution from the contact force to the energy equation can be written as

$$\left(\frac{\mathrm{d}e_a}{\mathrm{d}t}\right)_{\mathrm{cont}} = -\sum_{b=1}^{N_{\mathrm{cont}}} \frac{(\mathbf{v}_b - \mathbf{v}_a)}{2} V_a V_b K_{\mathrm{ca}} n_{\mathrm{ca}} \frac{W_{ab}^{n_{\mathrm{ca}}-1}}{W(\Delta p)^{n_{\mathrm{ca}}}} \nabla_a W_{ab} \tag{16}$$

3. Numerical examples

3.1. Coupled artificial stress demonstration

The test presented by Swegle et al. [5] was recreated here in order to highlight the effectiveness of artificial stress with the Eulerian mixed kernel-and-gradient correction formulation and the coupled mixed kernel-and-gradient correction methods. Swegle et al. highlighted the tensile instability by applying a velocity perturbation to a single particle in a stationary two-dimensional square body of size 0.02×0.02 [m^2]. They discretised the domain using a uniform particle spacing of $\delta x = 0.001$ m and applied a velocity of $v = 1$ μm/s. Swegle et al. pointed out that a compressive stress does not alter particle positions as the initial velocity perturbation is small. Additionally, they noted that a tensile stress leads to the instant clumping of particles and the creation of voids. They noted this phenomenon regardless of whether the problem was run in one, two or three dimensions.

In this example, a 1×1 [m^2] square body was discretised by 100×100 particles. The initial condition was a uniform pressure of 10 Pa, applied to a patch of size 0.5×0.5 [m^2] in the centre of the body. The pressure was initially 0 Pa elsewhere in the domain. Unlike Swegle et al. [5] or Reveles [31] the boundary particles were not fixed and the domain was free to contract and expand periodically, much like in the patch test explored by Ganzenmüller [32]. A schematic of this test is displayed in Figure 3.

The Cauchy stress tensor is defined as $\boldsymbol{\sigma} = \boldsymbol{\sigma}' - p\mathbf{I}$. Therefore, in this test the initial condition for both the Cauchy stress and first Piola-Kirchhoff stress was $\boldsymbol{\sigma} = \mathbf{P} = -p\mathbf{I}$. The material was
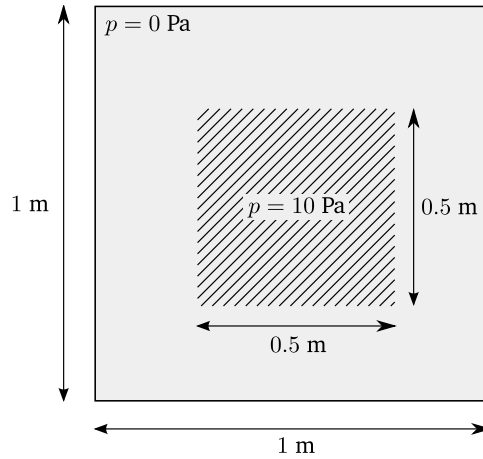
14

Figure 3: Schematic of the two-dimensional tensile instability test. An initial condition of tensile pressure of 10 Pa is applied to the central patch of size 0.5 m × 0.5 m.

modelled as linear elastic with density $\rho = 1 \, \mathrm{kg/m^3}$, Young's modulus $E = 1$ Pa and Poisson's ratio $\nu = 0.3$. As this test was intended to be illustrative rather than physical, the material parameters were not of great importance. The cubic spline kernel was used, following Swegle et al. [5]. The smoothing length was fixed with $h = 1.2\delta x$. Artificial viscosity was implemented with the parameters set to $\alpha = 0.2$ and $\beta = 0.4$. The time step was calculated to be $\Delta t = 2.59$ ms. This test was simulated using a Total Lagrangian and an Eulerian mixed kernel-and-gradient correction formulation and Figure 4 shows the results of both after 180 steps or 0.46 s. From these results it is clear that the Total Lagrangian formulation remained stable whilst the Eulerian formulation exhibited the tensile instability. This is evident due to the clear clumping of particles and the voids that formed. Following the snapshot in Figure 4(b), the Eulerian simulation became unstable due to the growth of particle velocity caused by the tensile instability.

The mixed kernel-and-gradient correction formulation of artificial stress, as detailed in Section 2.1, was then applied to the Eulerian particles. The artificial stress parameters were set to $n_{\mathrm{as}} = 4$ and $\epsilon_{\mathrm{as}} = 0.3$. These values were selected as Gray et al. [8] found that $n_{\mathrm{as}} = 4$ was best when using the cubic spline function as it restricts the impact of artificial stress to nearest neighbours. Figure 5 compares the pressure found using the Total Lagrangian formulation to that found using the Eulerian formulation with artificial stress after 500 time steps or 1.29 s. Although the tensile instability was much reduced, some clumping is still visible. It is also noted that the

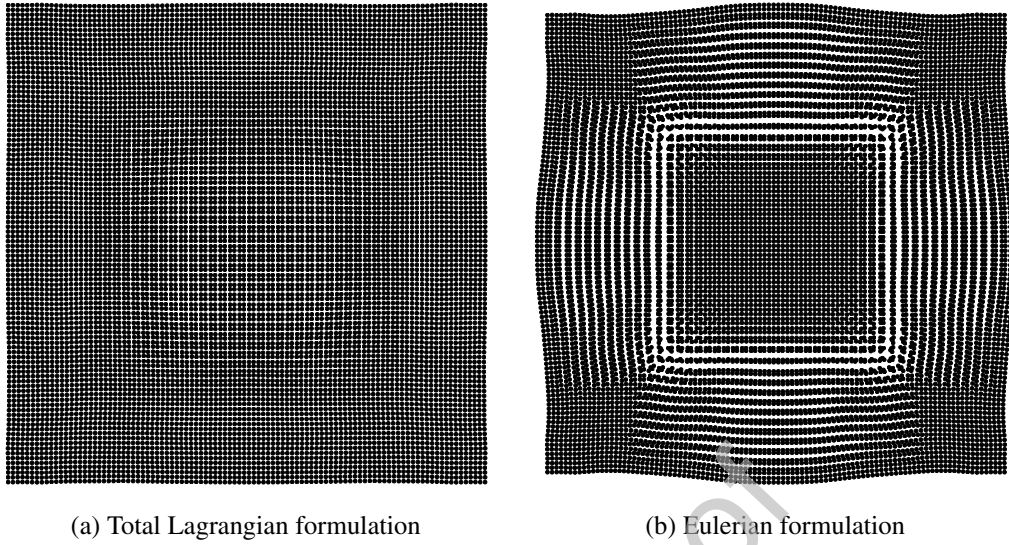(a) Total Lagrangian formulation   (b) Eulerian formulation

Figure 4: Particle positions of the (a) Total Lagrangian formulation and (b) the Eulerian formulation both with mixed kernel-and-gradient correction and artificial viscosity ($\alpha = 0.2$ and $\beta = 0.4$) after 0.46 s. The Eulerian formulation exhibits the tensile instability as shown by the particle clumping and voids.

maximum pressure was approximately 2.23 times larger in the Eulerian formulation with artificial stress than in the Total Lagrangian formulation. This was most likely due to the excessive stress that was introduced through artificial stress. The minimum pressures were similar, differing by approximately 12%. In both cases, the deformed shapes were similar. The Eulerian formulation was re-tested with $n_{as} = 3$ and $n_{as} = 2$. The results were not presented here due to the similarity with $n_{as} = 4$. It was observed that for $n_{as} = 3$ and $n_{as} = 2$ the void increased in size. Considering that n_{as} controls the range over which the artificial stress operates, this would appear to be reasonable.

Having defined a benchmark using the Total Lagrangian formulation and the Eulerian formulation with artificial stress, the coupling methods were tested with artificial stress. This was done by splitting the domain horizontally into two halves. The top half was populated by particles with an Eulerian kernel and the bottom half by particles with a Total Lagrangian kernel. Artificial stress could be reasonably implemented in three different ways when used with the coupling method. Either no artificial stress could be used between the Eulerian and Total Lagrangian interface pairs, artificial stress could be used for both the Eulerian and Total Lagrangian interface pairs, or artificial stress could be calculated using both kernel types in the interface but only be applied to the

16

Particle Pressure (Pa)

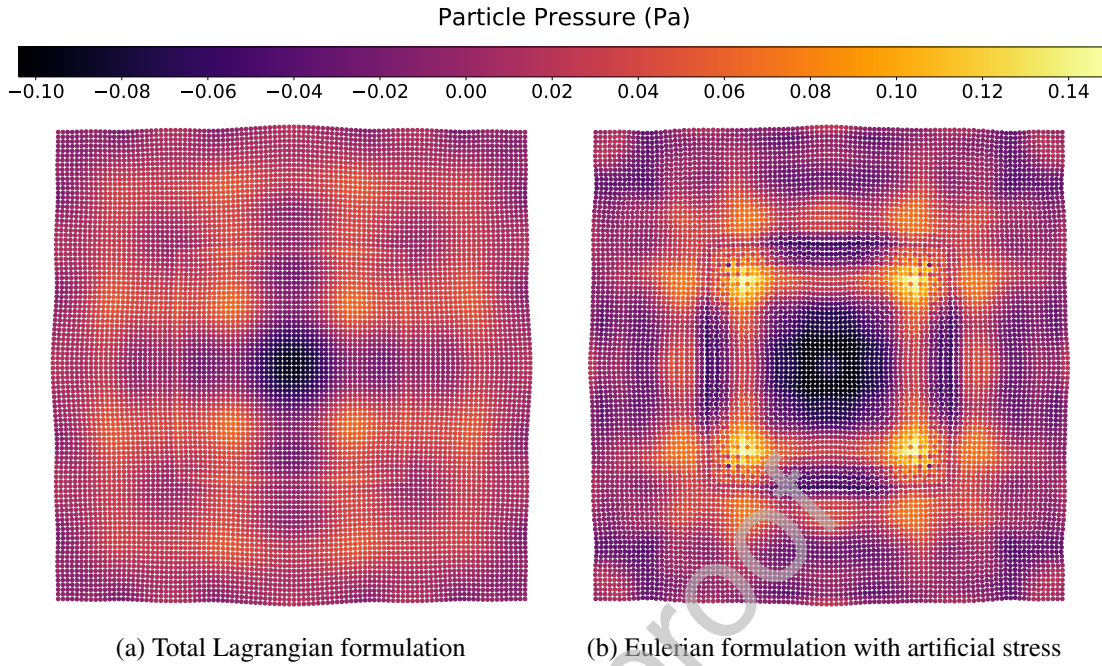(a) Total Lagrangian formulation　　　　(b) Eulerian formulation with artificial stress

Figure 5: Particle pressures calculated from the (a) Total Lagrangian formulation and (b) the Eulerian formulation with artificial stress ($n_{as} = 4$ and $\epsilon_{as} = 0.3$) after 1.29 s. Both formulations use mixed kernel-and-gradient correction and artificial viscosity ($\alpha = 0.2$ and $\beta = 0.4$). The Eulerian formulation no longer exhibits the tensile instability, although some slight clumping is still visible.

Eulerian particles. The third approach does not conserve momentum and energy as the pair-based values would not be equal and opposite. Regardless, all three approaches were tested and were found to produce highly similar results. The results for the second approach are shown in Figure 6.

No instabilities were found at the interface using this coupling method. The bottom half of the domain is similar to the Total Lagrangian simulation in Figure 6(a) and the top half of the domain is similar to the Eulerian simulation in Figure 6(b). The range of pressure values ($-0.09 - 0.12$ Pa) is slightly lower than for the non-coupled simulations ($-0.10 - 0.14$ Pa) but still in good agreement. Most importantly, the pressure can be seen to transition smoothly across the interface. The only notable difference between the three approaches, apart from minor differences in values of pressure (maximum difference of 3.6% in peak pressure), was that the third approach produced particles which were slightly shifted upwards by approximately 1.2 mm, most likely due to the unequal pairwise internal forces at the interface.
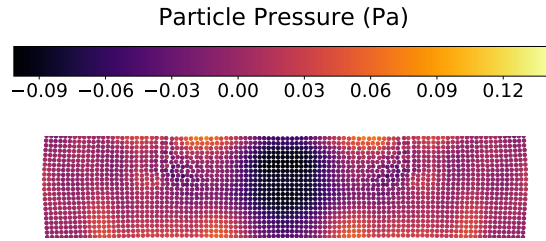
17

Particle Pressure (Pa)

Figure 6: Scatter plot coloured by particle pressure for a domain which is top half Eulerian and bottom half Total Lagrangian with the coupling method after 1.29 s. Mixed kernel-and-gradient correction and artificial viscosity ($\alpha = 0.2$ and $\beta = 0.4$) are used. Artificial stress ($n_{as} = 4$ and $\epsilon_{as} = 0.3$) is applied to Total Lagrangian particles in the interface as well as to Eulerian particles.

3.2. High-velocity impact problem

The Eulerian, mixed kernel-and-gradient correction, and AdapTLE formulations were evaluated for a two-dimensional high-velocity impact problem involving a circular projectile impacting on a rectangular target. The purpose of this numerical example was to validate the Eulerian formulation with mixed kernel-and-gradient correction for problems involving fracture and to highlight the effectiveness of the AdapTLE method. Howell and Ball [33] originally simulated the problem using a free-Lagrange Method. In the results presented here, the set-up was taken from Mehra and Chaturvedi [34] who applied different versions of the SPH method to the same problem.

The circular projectile had a diameter of $d = 1$ cm and initial velocity of $v_0 = 3100$ m/s. The rectangular target was $h = 5$ cm high and $w = 0.2$ cm wide. A schematic of the problem is shown in Figure 7(a).

Both the projectile and the target were modelled as aluminium with a density $\rho = 2785$ kg/m^3 and a shear modulus $G = 27.60$ GPa [33]. Howell and Ball [33] gave the bulk sound speed as $c_0 = 5328$ m/s, which was converted to a bulk modulus through $K = \rho c_0^2 = 79.06$ GPa. Using these values, the Young's modulus was calculated to be $E = 74.17$ GPa and the Poisson's ratio to be $\nu = 0.344$. Mehra and Chaturvedi [34] calculated the pressure using the following "stiffened gas" equation of state:

$$p = c_0^2(\rho - \rho_0) + (\gamma_0 - 1)\rho\frac{e}{m} \tag{17}$$

In this equation c_0 is the bulk sound speed, ρ and ρ_0 have their usual meanings, γ_0 is the Gruneisen
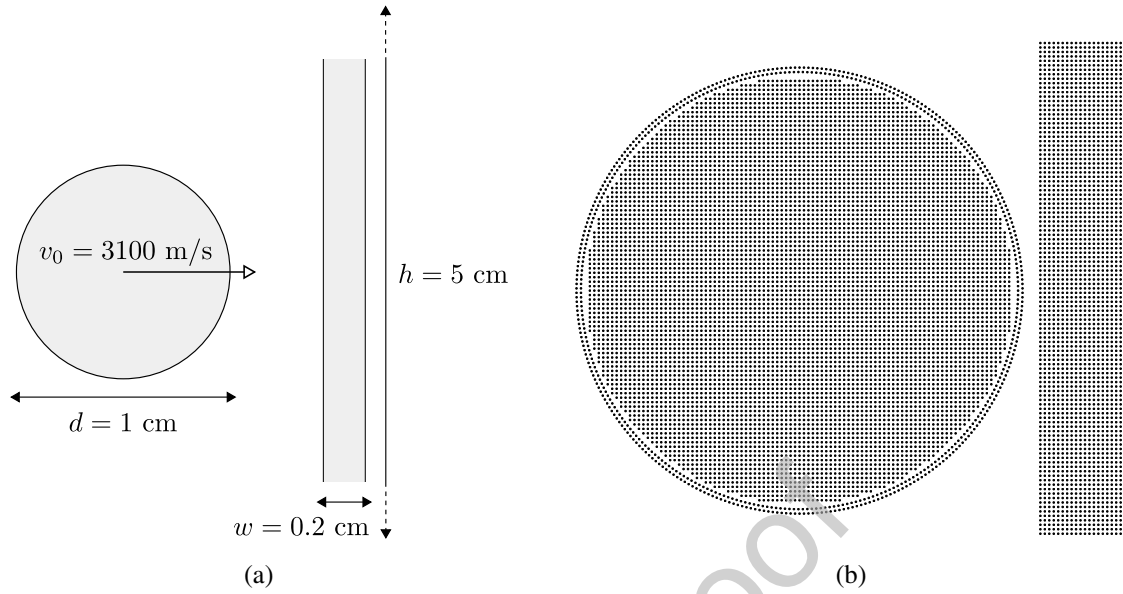
18

Figure 7: Two-dimensional high-velocity impact: (a) Schematic of the problem where an aluminium circular projectile impacts a stationary aluminium target with a velocity of 3, 100 m/s, and (b) the initial particle position where the circular projectile is populated by a rectangular distribution of particles encompassed by two rings of equally spaced particles. The circular projectile is formed by 7, 830 particles, which impact a rectangular target formed of 10, 020 particles. The full target is not shown in this figure.

parameter, e is the internal energy, and m is the mass. The value of $\gamma_0 = 2.0$ was taken from Howell and Ball [33]. Both the projectile and target were modelled as elastic-perfectly plastic with a yield stress of $\sigma_y = 0.3$ GPa.

Mehra and Chaturvedi [34] modelled the projectile and target using 17, 850 particles with a particle spacing of $\delta x = 0.01$ cm. These authors modelled the circular projectile using a rectangular grid for the majority of the body and two layers of particles arranged on the outer circumference of the projectile. The same particle set-up was used in this work and is shown in Figure 7(b).

Mehra and Chaturvedi [34] stated that they modelled the projectile using 7820 particles but this was assumed to be a typo as the projectile presented in Figure 7(b) contains 7830 particles and exactly matches the figure presented by these authors. In addition, it is noted that the particle spacing for the inner ring involves rounding down rather than rounding to the nearest integer. Subtracting the projectile leaves 10,020 particles for the rectangular target and it was therefore assumed that Mehra and Chaturvedi [34] modelled this as being 5.01 cm high. Mehra and Chaturvedi used a

19

smoothing length of $h = 1.4\delta x$ along with the cubic kernel function. This was replicated in the present work. As these authors modelled the impact problem using conventional Eulerian SPH, it is assumed that no contact algorithm was implemented and that the momentum was transferred from the projectile to the target though the conservation equations.

Mehra and Chaturvedi [34] modelled this problem using five types of SPH referred to as BAL, MON, CON, SAV1 and SAV2. SAV1 and SAV2 refer to conventional Eulerian SPH with artificial viscosity parameters $\alpha = 1$, $\beta = 2$ and $\alpha = 2.5$, $\beta = 2.5$. BAL referred to a scheme that made use of the Balsara switch. This switch was intended to prevent the use of excessive artificial viscosity. MON referred to a modification to artificial viscosity, as devised by Morris and Monaghan. Lastly, CON referred to an SPH formulation that solved the conservation equations by substituting a solution to the Riemann problem. In this work, the symmetrical Eulerian formulation with no correction was applied firstly to recreate SAV1. Figure 8 presents the particle positions of the upper half of the target and projectile $8\,\mu s$ after impact.

Only the upper half is required due to the problem symmetry. Impact was considered to commence in the time step when the support domains of the particles in the projectile and target overlapped. The results obtained by Mehra and Chaturvedi [34] using BAL, MON, CON, SAV1 and SAV2 and the results found using the Eulerian formulation presented in this work are shown in this figure. It is evident that: the recreated SAV1 and the SAV1 presented by Mehra and Chaturvedi are very similar; the tensile instability spoiled both solutions due to the clumping of particles and voids in the projectile and the target; and the Riemann-based method CON produced the most plausible results with no particle clumping or voids. It is also noted that the total energy grew by 0.048% after $8.68\,\mu s$ for the recreated SAV1. This was found to be acceptable considering that Zhang and Liu [35] noted an energy decrease of 3% after $20.00\,\mu s$ in their simulation of this problem, albeit at an impact speed of 6180 m/s and with gradient correction.

A number of changes were considered in order to improve the results. These included the use of artificial stress, imposing a contact algorithm rather than using kernel contact as discussed in Section 2.4, and the application of mixed kernel-and-gradient correction. These were evaluated in turn. Firstly, SAV1 was recreated with the inclusion of artificial stress with $\epsilon_{as} = 0.3$ and $n_{as} = 4$. Secondly, SAV1 was recreated using the contact algorithm with $K_{ca} = 2 \times 10^{12}$ and $n_{ca} = 4$.
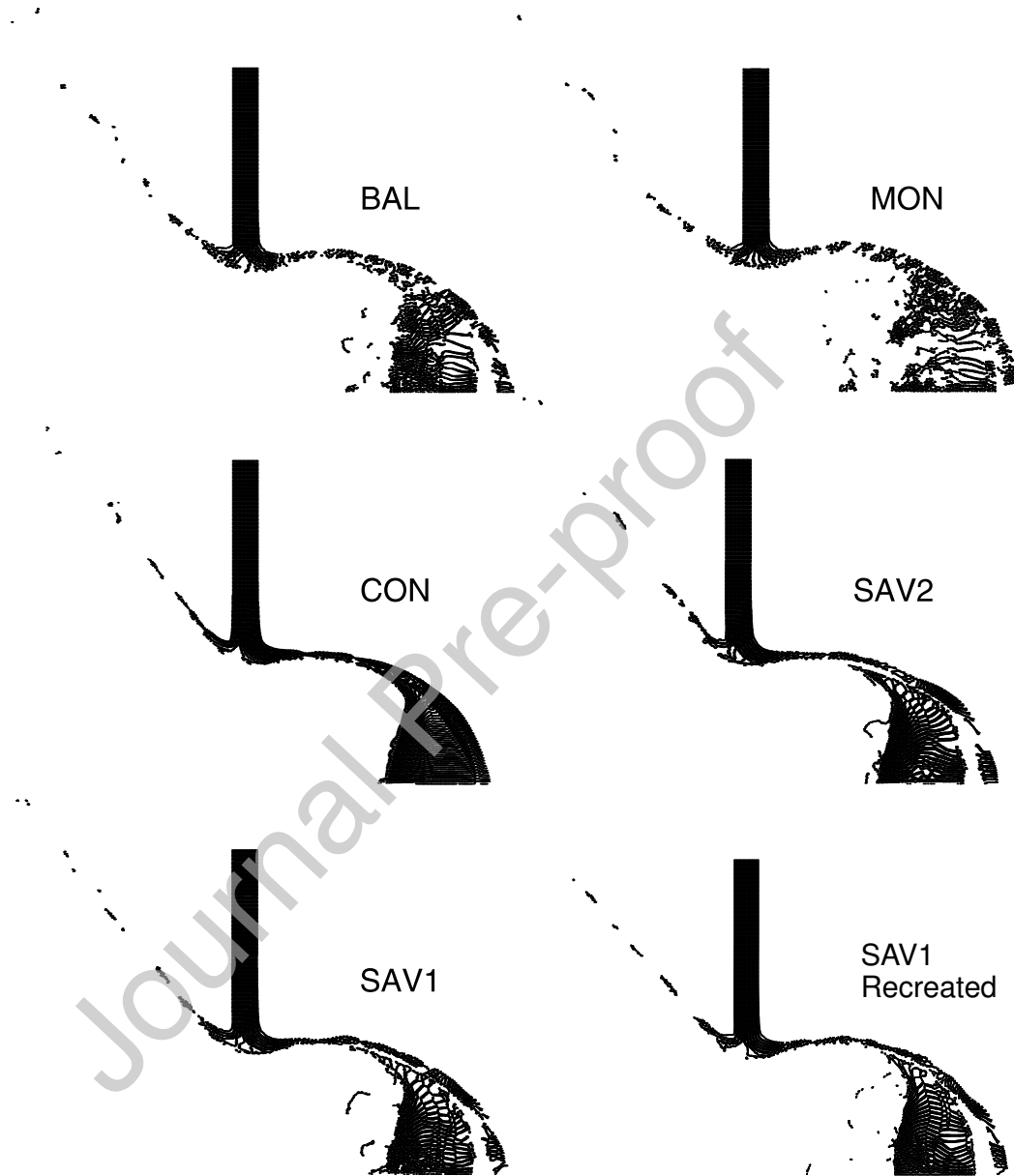
20

Figure 8: Particle positions of the high-velocity impact problem 8 μs after impact. Results for the BAL, MON, CON, SAV1 and SAV2 schemes are taken from Mehra and Chaturvedi [34]. The SAV1 scheme has been recreated to validate the Eulerian SPH formulation with no correction.

21

Thirdly, mixed kernel-and-gradient correction was used for the SAV1 scheme. The results of each are compared against the recreated SAV1 8 μs after impact and are presented in Figure 9.
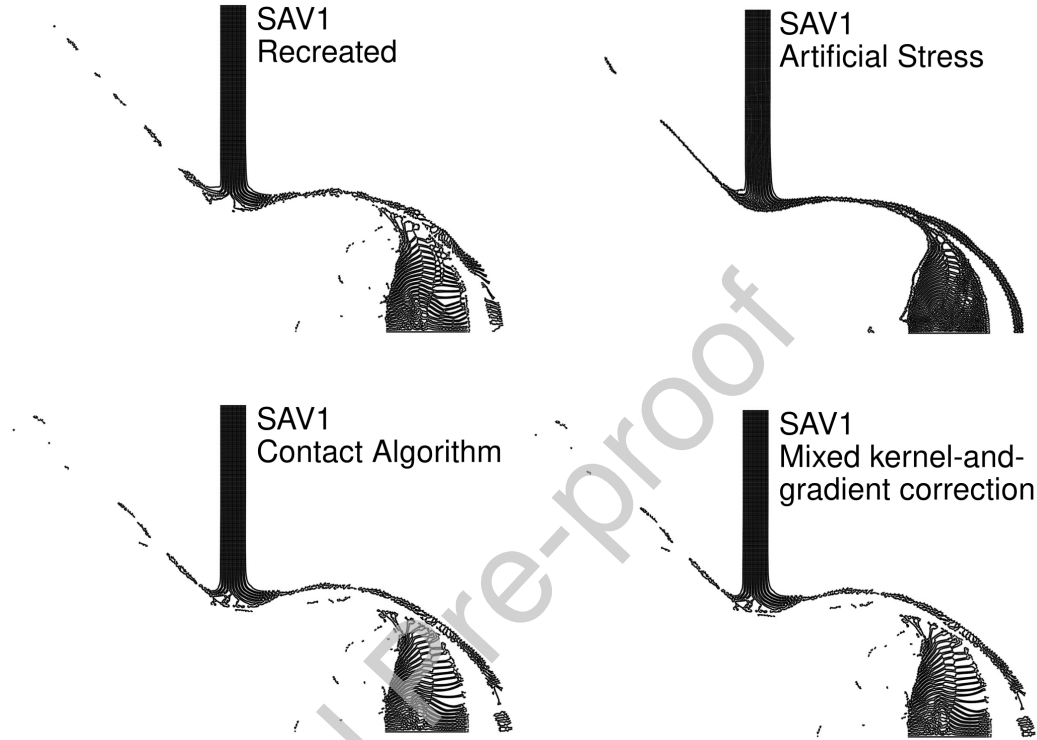

Figure 9: Particle positions of the high-velocity impact problem 8 μs after impact. The results are for the recreated SAV1 scheme from Mehra and Chaturvedi [34], SAV1 with artificial stress, SAV1 with the contact algorithm and SAV1 with the adapted mixed kernel-and-gradient correction.

The implementation of mixed kernel-and-gradient correction or gradient correction to simulations involving spallation is challenging. Spalled particles can have few, if any, nearest neighbours. Both the mixed kernel-and-gradient correction and gradient correction scheme are dependent on the inversion of a matrix (Equations 5). This matrix is formed by the volume-weighted sum of the gradient of the corrected kernel $\nabla \widetilde{W}$ with the particle positions $\mathbf{x}$. Consequently, if a particle should only have one neighbour this matrix becomes singular, resulting in a non-invertible matrix. Some arrangement of particles with two or three neighbours can also result in a correction matrix $\mathbf{K}$, which produced large accelerations, spoiling the solution.

Gradient correction, which is dependent on matrix inversion, can be applied to high-velocity

impact problems as demonstrated by Zhang and Liu [35], though it is not clear how these authors dealt with the accompanying spurious accelerations. In this work, the following adaptation is proposed. All particles with only one neighbour (excluding themselves) revert to the conventional kernel gradient. For all other particles, the corrected gradient of the corrected kernel is compared against the conventional kernel gradient. If the difference between any two corresponding elements in these vectors differs by a pre-determined factor C_f then the mixed kernel-and-gradient correction is neglected and the conventional kernel gradient is adopted. If the distance between particles is close to zero, in any dimension, then this rule is ignored for the corresponding element in the kernel gradient, as this will always be zero. The limiting factor was $C_f = 7.5$ in this case. Ideally, this factor would be large so as to implement mixed kernel-and-gradient correction wherever possible whilst preventing non-physical accelerations. It is immediately evident that this conversion from mixed kernel-and-gradient correction to conventional non-corrected SPH will destroy the scheme's conservation properties. It was speculated that this might be confined to the regions of spallation and that overall the effect would be minor.

In Figure 9, it can be seen that artificial stress improved the results. There was minor spallation from the target and the implementation of artificial stress largely succeeded at removing the particle clumps and voids. The only other scheme to achieve this was the Riemann based CON scheme by Mehra and Chaturvedi [34]. The CON scheme succeeded at maintaining particle order in the projectile whilst the SAV1 scheme with artificial stress displayed a larger degree of particle disorder. Voids and particle clumping are visible in the upper portion of the projectile, indicating that the use of artificial stress did not completely suppress the tensile instability, as corroborated by a later publication by Mehra et al. [36]. The contact algorithm did not noticeably affect the results other than increasing the target crater diameter. Although the application of mixed kernel-and-gradient correction reduced the void between the projectile and the target, it also caused spalled particles to clump together. Additionally, a void is visible near the centre of the projectile, which was caused by the tensile instability. In all other schemes this void was re-populated by particles but the mixed kernel-and-gradient correction scheme was unable to achieve this. The application of mixed kernel-and-gradient correction with a switch value of $C_f = 7.5$ resulted in an energy increase of 0.98%. Whilst this is significantly greater than the energy increase of 0.048% for the

23

recreated SAV1, it was still found to be within acceptable levels considering the low threshold applied to convert from the mixed kernel-and-gradient correction kernel gradient to the conventional kernel gradient.

Mehra and Chaturvedi [34] compared their results against those obtained by Howell and Ball [33] using the peak pressure in the projectile P, peak tension in the projectile, crater diameter d_{cra}, width of the projectile L_{extn} and the distance travelled by the projectile L_{proj}. The same metrics are used in Table 1 with the exception of the peak tension. This could not be captured due to the tensile instability that caused voids to form in the projectile prior to the reflected shock wave reaching the centre of the projectile. The original SAV1 results presented by Mehra and Chaturvedi [34] and the results obtained by Howell and Ball [33] are given in this table. The recreated SAV1 results appear to differ from the original SAV1. However, it is noted that the recreated SAV1 results are in agreement with those presented by Asadi Kalameh et al. [37], who also simulated this problem using Eulerian SPH. These authors gave no values for pressure. Additionally, Mehra and Chaturvedi [34] evaluated the peak pressure by using an SPH summation, whilst in Table 1 the pressure was taken on a particle basis from the equation of state. Consequently, the recreated SAV1 pressure should be larger as is has not been smoothed. Lastly, Mehra and Chaturvedi [34] quote their lengths to a precision of 0.1 cm. The attempts to improve upon SAV1 did not make any noteworthy changes to the results in Table 1. Artificial stress did not affect the geometric or pressure values and the contact algorithm increased the crater diameter and peak pressure. The mixed kernel-and-gradient correction also increased the peak pressure along with the projectile width and the distance travelled.

The mixed kernel-and-gradient correction scheme was combined with artificial stress. The inclusion of artificial stress allowed the mixed kernel-and-gradient correction factors to be raised to $C_{\mathrm{f}} = 90$. Figure 10 compares the results of the recreated SAV1 against the SAV1 scheme with artificial stress ($\epsilon_{\mathrm{as}} = 0.3$ and $n_{\mathrm{as}} = 4$) and mixed kernel-and-gradient correction ($C_{\mathrm{f}} = 90$).

From this figure, it is evident that the mixed kernel-and-gradient correction has prevented the voids caused by the tensile instability from closing. These voids are significantly larger than those seen in the other trials. Table 1 highlights the pressure and geometric values obtained using this combination. The addition of artificial stress does not affect these results, as was the case without

24

Table 1: Pressure and geometric data for the high-velocity impact problem. P is the peak pressure at the centre of the projectile behind the leftward travelling shock wave, d_{cra} is the crater diameter, L_{extn} is the longitudinal extension (width) of the projectile and L_{proj} is the longitudinal distance travelled by the projectile measured from the leading edge. d_{cra}, L_{extn} and L_{proj} are measured 8 μs after impact.

Simulation	P (GPa)	d_{cra} (cm)	L_{extn} (cm)	L_{proj} (cm)
SAV1 [34]	18.0	2.0	0.7	1.8
B&H [33]	18.6	1.9	0.7	2.0
SAV1 recreated	19.4	2.1	0.6	1.9
SAV1 Artificial stress[a]	19.4	2.1	0.6	1.9
SAV1 Contact algorithm[b]	19.5	2.2	0.6	1.9
SAV1 Mixed kernel-and-gradient correction[c]	19.5	2.1	0.7	2.0
SAV1 Mixed kernel-and-gradient correction + Artificial stress[d]	19.5	2.1	0.8	2.0
SAV1 Artificial stress[a] + Contact algorithm[b] + Kernel adaptive conversion (AdapTLE)	20.9	2.2	0.7	1.9

[a] Artificial stress ($\epsilon_{as} = 0.3$ and $n_{as} = 4$)

[b] Contact algorithm ($K_{ca} = 2 \times 10^{12}$ and $n_{ca} = 4$)

[c] Mixed kernel-and-gradient correction ($C_f = 7.5$)

[d] Mixed kernel-and-gradient correction and artificial Stress ($\epsilon_{as} = 0.3$, $n_{as} = 4$ and $C_f = 90.0$)

the mixed kernel-and-gradient correction, with the exception of the longitudinal extension that has increased. In this simulation, the total energy increased by 0.136%, which was a significant reduction from the increase of 0.98% with $C_f = 7.5$. From these trials it would appear that, although the mixed kernel-and-gradient correction removes the void between the projectile and the target, the combination of artificial viscosity and artificial stress produced the results most similar to CON.

It is clear that although artificial stress aids in suppressing it, the tensile instability is still present in this problem. Therefore, AdapTLE was used to model the high velocity impact problem, where Total Lagrangian particles adaptively converted to Eulerian particles as discussed in

Figure 10: Particle positions of the high-velocity impact problem 8 μs after impact. The results are for the recreated SAV1 scheme from Mehra and Chaturvedi [34] and SAV1 combined with artificial stress and the adapted mixed kernel-and-gradient correction.

Section 2.3. The distribution of particles in the projectile had to be modified as the two outer layers of particles on the circumference penetrated the projectile upon impact. This was due to the low number of neighbours in the reference state. The particles in the projectile were therefore arranged by keeping an approximate arc and radial distance of 0.1 mm between particles, resulting in 8,012 particles. SAV1 with artificial stress with parameters $\epsilon_{as} = 0.3$ and $n_{as} = 4$ was recreated. As no damage criterion was used in this problem, particles changed kernel type when the equivalent strain

$$\bar{\epsilon} = \sqrt{\frac{2}{3}\boldsymbol{\epsilon}' : \boldsymbol{\epsilon}'} \tag{18}$$

exceeded a value of 0.85. Note that this problem was under plane stress conditions and consequently the out-of-plane strain had to be calculated as

$$\epsilon_{33} = -\frac{\nu}{E}(\sigma_{xx} + \sigma_{yy}) \tag{19}$$

As the domain was initially modelled with Total Lagrangian particles, the contact algorithm was used with $K_{ca} = 2 \times 10^{12}$ and $n_{ca} = 4$. The results for the AdapTLE coupling method, at 2, 4, 6 and 8 μs after impact are displayed in Figure 11 and are coloured by particle kernel type.

The particles that changed from Total Lagrangian to Eulerian kernel type are represented by the lighter colour. A number of comments can be made if comparing these results to those obtained by Mehra and Chaturvedi [34] in Figure 8 and the further trials shown in Figure 10. The crater
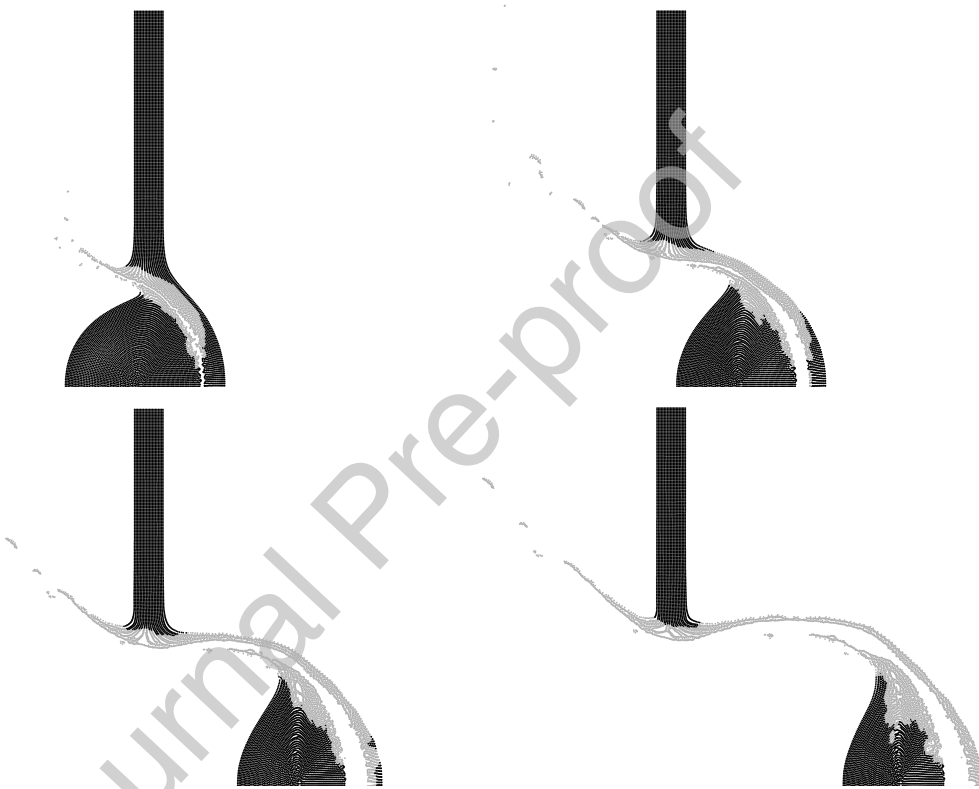
26

Figure 11: Particle positions of the high-velocity impact problem 2, 4, 6 and 8 μs after impact. The results are for the recreated SAV1 scheme from Mehra and Chaturvedi [34] modelled using AdapTLE, where Total Lagrangian kernel types (black) adaptively converted to Eulerian kernel types (grey).

27

diameter is less circular. This was most likely caused by the progressive change of particles from Total Lagrangian to Eulerian in the crater, which led to a different response to the tensile stresses. There is a larger void between the projectile and the crater. This can be largely attributed to the use of the contact algorithm, as previously seen. Perhaps most interesting is the final shape of the deformed projectile. As the majority of the back of the projectile remained Total Lagrangian, the particles are still ordered, as in the CON simulation. Additionally, particles do not spall from the back of the projectile due to the Total Lagrangian formulation, in combination with the different particle arrangement. The tensile instability can be seen to manifest in the Eulerian particles as in the previous simulations. The geometric and pressure values for the adaptive simulation are listed in Table 1. It is not strictly correct to compare simulations with different initial particle arrangements as the adaptive simulation contained nearly 200 more particles in the projectile that the previous simulations. Using this adaptive particle conversion, it was possible to capture the pressure wave as it reflected, unlike in the previous Eulerian simulations. The peak tension in the projectile after the reflection of the initial pressure was found to be 22.5 GPa at 2.3 μs after impact. In comparison, Mehra and Chaturvedi [34] found this to be 18.5 GPa at 2.2 μs after impact. Higher pressures may be seen in the adaptive simulation due the larger mass of the projectile caused by the additional particles.

3.3. Three-dimensional debris impact

In this problem, AdapTLE was applied to a three-dimensional debris impact simulation. This involved a spherical projectile impacting a stationary square target. The problem set-up was taken from Reveles' PhD thesis [31] with a number of amendments. The projectile was modelled as a 12 mm diameter steel sphere with an initial velocity of v_0 = 500 m/s and the plate as aluminium with height 100 mm, width 100 mm and thickness 3 mm. A schematic of the configuration is presented in Figure 12. The particles along the 3 mm thick outer surfaces of the plate were clamped such that they did not experience any displacement.

The material properties for aluminium were given by ρ = 2870 kg/m^3, E = 70 GPa, v = 0.33 and σ_y = 479 MPa. The plastic response of the aluminium target was captured using the Johnson-Cook plasticity model [38]. The Johnson-Cook parameters were given by A_{JC} = 479 MPa, B_{JC} =
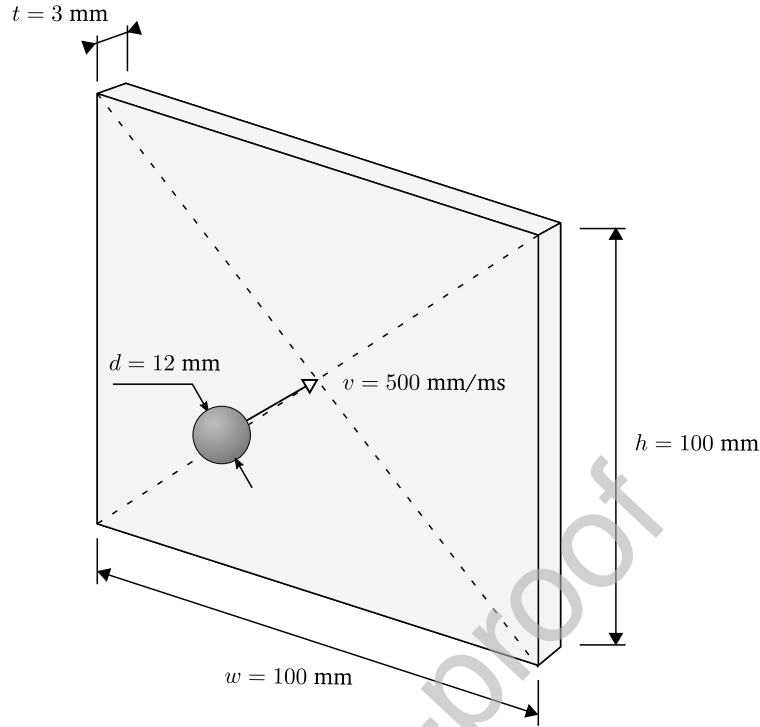
28

Figure 12: Schematic of the debris impact problem. A spherical piece of debris with diameter 12 mm travels at 500 m/s perpendicularly to a square metal plate of dimensions $100 \times 100 \times 3$ [mm^3], which is clamped along its edges.

323 MPa, $C_{JC} = 0.101$, $\dot{\epsilon}_0 = 1.0$ s^{-1}, $M_{JC} = 1.80$, $N_{JC} = 0.410$, $T_r = 300$ K, $T_m = 850$ K and $C_v = 875$ J/(kgK). The Johnson-Cook damage model [39] was also used with $D_1 = 0.45$, $D_2 = 0$, $D_3 = 0$, $D_4 = 0.0138$ and $D_5 = 0$. The commercial software LS-DYNA® provides three spall models, if using the Johnson-Cook damage model. Reveles [31] made use of the "pressure limit model", which places a restriction, p_{min}, on the minimum value of tensile pressure. Note that this presumes a convention where tensile pressure is negative. Any pressures which are more tensile that this value are reset to p_{min}. Following Reveles, the minimum tensile pressure was set to $p_{min} = -800$ MPa. The pressure in the aluminium plate was calculated using the cubic Hugoniot form of the Mie-Gruneisen equation of state [40] with parameters $c = 5328$ m/s, $\gamma_0 = 2$, $a_{mg} = 0.480$, $s_1 = 1.338$, $s_2 = 0$ and $s_3 = 0$.

The material properties for steel were given by $\rho = 7870$ kg/m^3, $E = 200$ GPa, $v = 0.30$ and $\sigma_y = 315$ MPa. The steel debris was modelled as elastic-plastic with isotropic hardening using a plastic modulus of $E_p = 16.2$ GPa. Damage was not considered for the debris. The pressure was

29

calculated using the elastic equation of state.

Both the plate and debris were modelled using an inter-particle spacing $\delta x = 1$ mm, resulting in 912 particles in the debris and 30,000 particles in the plate. The particles in the debris only approximated the sphere as they were distributed on a cubic lattice. Artificial viscosity was used with parameters $\alpha = 1.0$ and $\beta = 2.0$. These values were chosen as they were found to be effective in the impact problem previously discussed in Section 3.2. The smoothing length was set to $h = 1.2\delta x$. Lastly, the contact algorithm was used between the debris and plate with $K_{ca} = 1 \times 10^{16}$ and $n_{ca} = 4$. The following four combinations of particle kernel types were investigated:

- both the debris and target were modelled using Eulerian particles (EUL),

- both the debris and target were modelled using Total Lagrangian particles (TLAG),

- both the debris and target were modelled using Total Lagrangian particles and a central patch of the plate of size $16 \times 16 \times 3$ [mm^3] was modelled using Eulerian particles (PATCH), and

- both the debris and target were modelled using Total Lagrangian particles. Particles in the target used AdapTLE to adaptively convert to an Eulerian kernel type once damaged (AdapTLE). A discussion on this adaptive particle conversion is given in Section 2.3.

Simulations EUL and TLAG were included as limiting cases considering that EUL will suffer from the tensile instability and TLAG will require that damaged particles have their field variables set to zero and are deleted from neighbour lists, in order to model fracture. This too is discussed in Section 2.3. The mixed kernel-and-gradient correction was not applied in this example as it was found to complicate the previous high-velocity impact problem in Section 3.2. Note that if a particle converted type in the adaptive simulation with the coupling method, AdapTLE, a large number of neighbours were also required to convert type. This was because this problem was three-dimensional and if this was not done, Total Lagrangian particles had Eulerian neighbours with non-physical deformation gradients.

Figure 13 presents a three-dimensional view of the particles' locations and kernel types 153 μs after impact and Figure 14 shows cross-sections of the domains. Neither of these figures display the wholly Eulerian simulation (EUL) as the results were visually indistinguishable from the
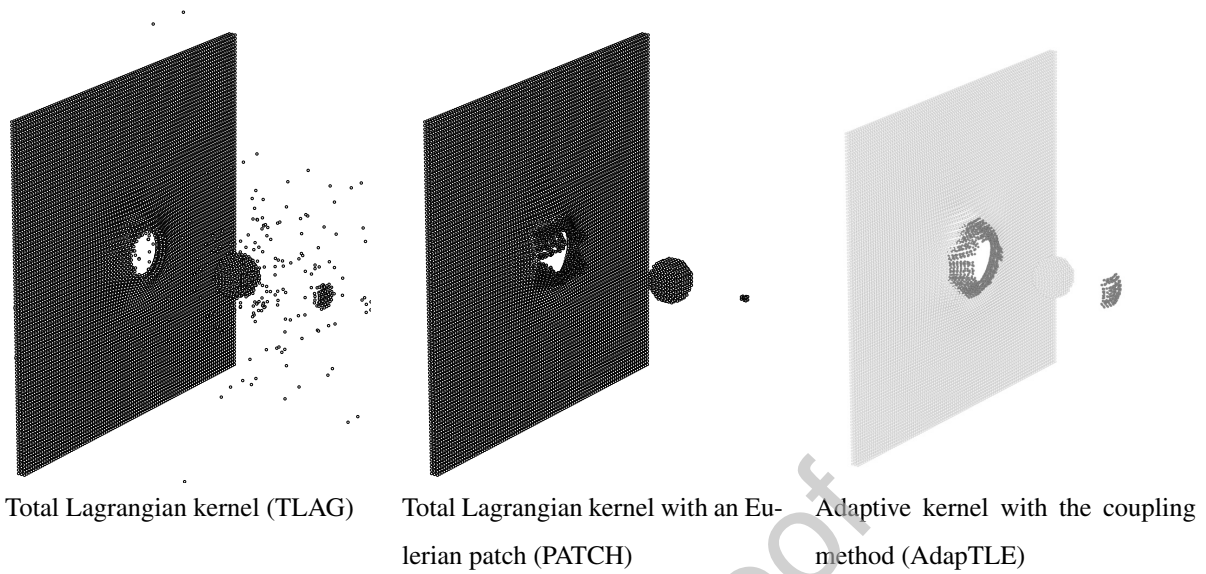
30

Total Lagrangian kernel (TLAG)   Total Lagrangian kernel with an Eu-   Adaptive kernel with the coupling
                                   lerian patch (PATCH)   method (AdapTLE)

Figure 13: Three-dimensional view of the particle positions and kernel types 153 μs after impact. The darker colour represents particles with an Eulerian kernel and the lighter colour represents particles with a Total Lagrangian kernel.

simulation with the Eulerian patch (PATCH). From these figures, it would appear that both the Eulerian simulation (EUL) and the Total Lagrangian simulation with the Eulerian patch (PATCH) were dominated by petalling with minor plugging and no spallation. It is speculated that this was driven by the tensile instability, which, upon impact, caused the particles to clump together along either side of the axis of symmetry. This may have been influenced by the regular grid arrangement of particles in the plate. The Total Lagrangian simulation (TLAG) produced a larger plug that the previously mentioned simulations but conversely produced no petalling and a very large degree of spallation. The adaptive simulation with the coupling method (AdapTLE) produced the largest plug along with no spallation and minor petalling. As stated by Reveles [31], plugging and petalling are typical of low velocity impact on ductile materials, rather than spallation. For this reasons, it would appear that the adaptive conversion of particle kernel types produced the most plausible results.

An attempt was made to implement a three-dimensional form of artificial stress in the Eulerian simulations. This implementation has not been well covered in the literature. The approach attempted in this work was to extend the theory detailed in Section 2.1 to three dimensions by finding the eigenvalues and eigenvectors of the Cauchy stress tensor. The principal components
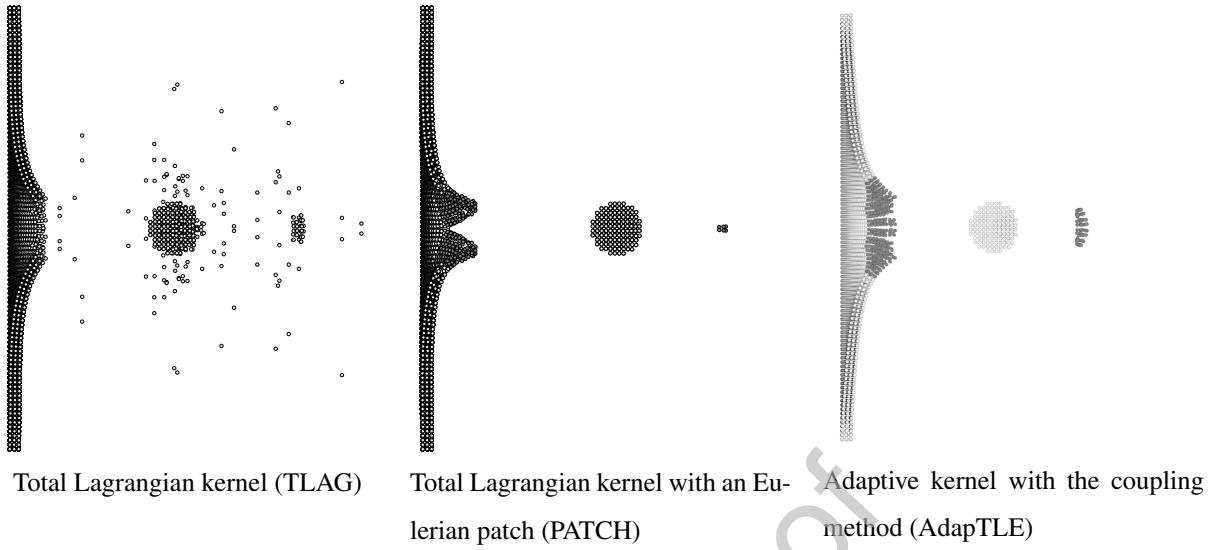
31

Total Lagrangian kernel (TLAG) Total Lagrangian kernel with an Eu- Adaptive kernel with the coupling
lerian patch (PATCH) method (AdapTLE)

Figure 14: Cross-sections of the particle positions and kernel types 153 μs after impact. The darker colour represents particles with an Eulerian kernel and the lighter colour represents particles with a Total Lagrangian kernel.

were then modified, if tensile, and then rotated back to their original directions, as in Section 2.1. This produced significantly more spalled particles with no discernible plug. Therefore, the three-dimensional implementation of artificial stress was not investigated further.

Table 2 compares the post-impact velocity of the debris v_d and the plug v_p, the impact diameter d_i, the plug width w_p and the plate lip height h_{pl}, 153 μs after impact.

Table 2: Geometric data for the three-dimensional debris impact problem using four combinations of kernel types. v_d and v_p are the post-impact velocities of the debris and plug, d_i is the impact diameter, w_p is the plug width and h_{pl} is the plate lip height. All measurements were taken 153 μs after impact.

Simulation	v_d (mm/ms)	v_p (mm/ms)	d_i (mm)	w_p (mm)	h_{pl} (mm)
Eulerian (EUL)	324	463	13.32	0.88	9.76
Total Lagrangian (TLAG)	270	443	13.92	5.88	5.69
Eulerian patch (PATCH)	319	449	13.44	0.88	9.79
Adaptive kernel (AdapTLE)	257	373	14.08	8.38	10.16
FEM	299	343	14.20	8.75	8.71

The impact diameter was measured as twice the average radius of the particles at the outermost

32

edges of the plate lip. The plate lip height was measured as the perpendicular distance between a fixed edge particle along the outer face of the plate and a particle on the outermost edges of the lip. The simulation involving particle conversion, (AdapTLE), produced the lowest post-impact debris and plug velocities. This was expected considering that both the simulations that made use of the Eulerian kernel (EUL) and the Eulerian patch (PATCH) would be expected to manifest the tensile instability, resulting in particle clumping and less resistance to the passage of the debris. Similarly, the simulation that made use of the Total Lagrangian kernel (TLAG) would offer lesser resistance to the debris considering that, once damaged, the particles had their field variables set to zero. Both EUL and PATCH gave similar crater diameters as both simulations displayed the artificial petalling. The Total Lagrangian simulation (TLAG) produced a comparatively large crater diameter, most likely due to the excessive spallation. The adaptive simulation with the coupling method (AdapTLE) produced the largest crater diameter. Again, EUL and PATCH gave very similar plate lip heights, whilst TLAG displayed the smallest lip height, again due to the spallation. The adaptive simulation (AdapTLE) produced the largest lip height, though this was similar to the Eulerian (EUL) and (PATCH) patch simulations.

Lastly, the SPH formulations discussed were compared against a Finite Element Analysis (FEA) carried out in LS-DYNA®. The same material properties and plasticity and damage models were used in both the SPH code and LS-DYNA®. As the finite elements could not naturally capture fracture (unlike the AdapTLE method), elements were eroded based on the damage criteria defined by the Johnson Cook material card (MAT015 [41]). In order to successfully capture erosion, six elements were required along the thickness of the plate. Figure 15 presents a cross-section and three-dimensional view of the Finite Element analysis 153 µs after impact.

Comparing the SPH and Finite Element Method (FEM) cross-section and three-dimensional views, it is evident that the AdapTLE method was the most similar to the FEM with no spallation and a discernible plug. The results from the FEM have been included in Table 2. Again, the AdapTLE method produced the most similar results to the FEM, where the percent error relative to the FEM was $\delta v_d = 14\%$, $\delta v_p = 9\%$, $\delta d_i = 1\%$, $\delta w_p = 4\%$, and $\delta h_{pl} = 17\%$. This $h_{pl} = 17\%$ error in the plate lip height can be explained by the erosion of elements in the FEM. Though, as the elements are curving out and away from the plate, it is likely that the element erosion will have had
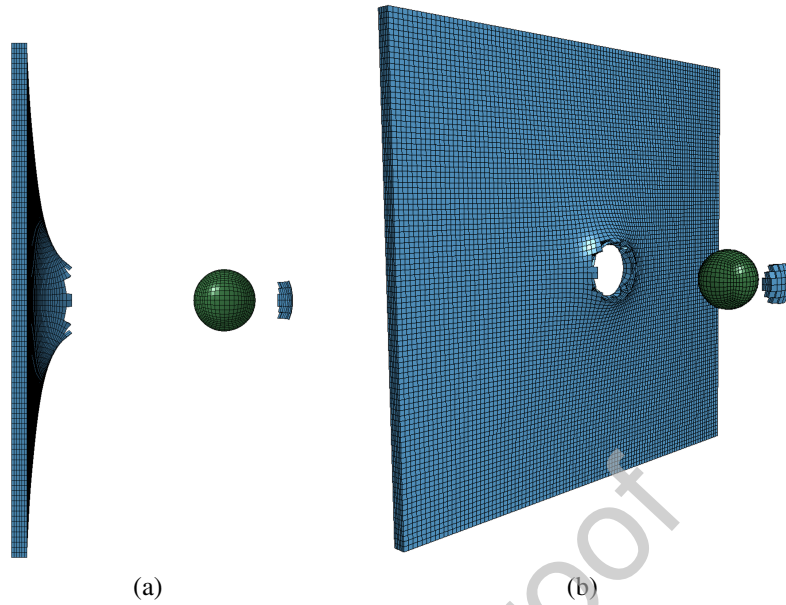
33

(a)   (b)

Figure 15: (a) Cross-section and (b) three-dimensional view of the debris impact problem 153 µs after impact, modelled using Finite Elements.

a lesser effect on the impact diameter. Although the percentage error in the post-impact velocity of the debris is $\delta v_{\mathrm{d}} = 14\%$, this should not be considered in isolation as the post impact velocities are directly related. The AdapTLE method produced the lowest average percentage error in the post-impact velocities of $(\delta v_{\mathrm{d}} + \delta v_{\mathrm{p}})/2 = 11\%$.

This numerical example highlighted how the adaptive conversion of kernel particle types can aid in the simulations of high-velocity impact and fracture using SPH. The AdapTLE simulation produced superior results to the simulations that made use of one kernel type or a predetermined patch of Eulerian particles and produced the most similar results to the Finite Element Method both qualitatively and quantitatively.

4. Conclusions

This work presented a novel coupling between the Eulerian and Total Lagrangian formulations and applied it to high-velocity impact problems. To do so, both artificial viscosity and artificial stress were added to the formulation, and a novel form of artificial viscosity was presented for the Total Lagrangian formulation. Mixed kernel-and-gradient correction was used to improve

34

consistency and a coupling methodology was explored. The strength of the proposed methodology was shown though three numerical examples, which have not been simulated before using this novel approach. These included:

1. The coupled artificial stress demonstration showed how the Eulerian formulation suffers from tensile instability and also how this can be partially relieved through artificial stress. More importantly, it showed how the coupling methodology proposed in this paper can be used to smoothly transition from a Eulerian to a Total Lagrangian formulation. It was found that artificial stress can be implemented in three ways at the interface. The demonstration suggests that either no artificial stress should be used between then Eulerian-Total Lagrangian interface pairs or it should be applied to both particles in the interface pair (but not exclusively to the Eulerian particle in the interface pair).

2. A two-dimensional high velocity impact problem was revisited, and the developments of this paper were applied. It was found that, for a Eulerian formulation, the artificial stress cannot subdue the tensile instability and that the reflected pressure wave in the projectile is difficult to capture. Using an AdapTLE approach, where the particles converted from a Total Lagrangian to an Eulerian formulation, was found to produce much improved results where the projectile maintained its ordered particle positions and the reflected wave could be captured.

3. Lastly, a three-dimensional debris impact problem combined the formulations in four different ways. It was shown how the Total Lagrangian formulation could not manage large distortions of the reference state and how, yet again, the tensile instability spoiled the solution for an Eulerian formulation. The AdapTLE approach was found to produce the most similar results to a Finite Element Analysis, where the maximum discrepancy was 17% in the plate lip height and can be explained by the erosion of elements.

Acknowledgements

Conflicts of interest: none

References

[1] R. A. Gingold, J. J. Monaghan, Smoothed particle hydrodynamics: theory and application to non-spherical stars, Mon. Not. R. Astron. Soc. 181 (3) (1977) 375–389. `doi:10.1093/mnras/181.3.375`.

[2] L. B. Lucy, A numerical approach to the testing of the fission hypothesis, Astron. J. 82 (12) (1977) 1013. `arXiv:9809069v1`, `doi:10.1086/112164`.

[3] M. B. Liu, G. R. Liu, Smoothed particle hydrodynamics (sph): an overview and recent developments, Arch. Comput. Methods Eng. 17 (1) (2010) 25–76. `doi:10.1007/s11831-010-9040-7`.

[4] L. D. Libersky, A. G. Petschek, Smooth particle hydrodynamics with strength of materials, in: H. Trease, M. Fritts, W. Crowley (Eds.), Advances in the Free-Lagrange Method Including Contributions on Adaptive Gridding and the Smooth Particle Hydrodynamics Method, Vol. 395 of Lecture Notes in Physics, Berlin Springer Verlag, Springer Berlin Heidelberg, Berlin, Heidelberg, 1991, pp. 248–257. `doi:10.1007/3-540-54960-9_58`.

[5] J. W. Swegle, D. L. Hicks, S. W. Attaway, Smoothed particle hydrodynamics stability analysis, J. Comput. Phys. 116 (1) (1995) 123–134. `doi:10.1006/jcph.1995.1010`.

[6] C. T. Dyka, R. P. Ingel, An approach for tension instability in smoothed particle hydrodynamics (sph), Comput. Struct. 57 (4) (1995) 573–580. `doi:10.1016/0045-7949(95)00059-P`.

[7] J. J. Monaghan, Sph without a tensile instability, J. Comput. Phys. 159 (2) (2000) 290–311. `doi:10.1006/jcph.2000.6439`.

[8] J. P. Gray, J. J. Monaghan, R. P. Swift, Sph elastic dynamics, Comput. Methods Appl. Mech. Eng. 190 (49-50) (2001) 6641–6662. `doi:10.1016/S0045-7825(01)00254-7`.

[9] J. Bonet, S. Kulasegaram, Remarks on tension instability of eulerian and lagrangian corrected smooth particle hydrodynamics (csph) methods, Int. J. Numer. Methods Eng. 52 (11) (2001) 1203–1220. `doi:10.1002/nme.242`.

[10] T. Belytschko, W. K. Liu, B. Moran, K. Elkhodary, Nonlinear Finite Elements for Continua and Structures, 1st Edition, Wiley, Chichester, 2000.

[11] T. Rabczuk, T. Belytschko, Cracking particles: a simplified meshfree method for arbitrary evolving cracks, Int. J. Numer. Methods Eng. 61 (13) (2004) 2316–2343. `doi:10.1002/nme.1151`.

[12] J. Bonet, S. Kulasegaram, Alternative total lagrangian formulations for corrected smooth particle hydrodynamics (csph) methods in large strain dynamic problems, Rev. Eur. des Éléments Finis 11 (7-8) (2002) 893–912. `doi:10.3166/reef.11.893-912`.

[13] J. Bonet, T. S. L. Lok, Variational and momentum preservation aspects of smooth particle hydrodynamic formulations, Comput. Methods Appl. Mech. Eng. 180 (1-2) (1999) 97–115. `doi:10.1016/S0045-7825(99)00051-1`.

[14] M. Basa, N. J. Quinlan, M. Lastiwka, Robustness and accuracy of sph formulations for viscous flow, Int. J. Numer. Methods Fluids 60 (10) (2009) 1127–1148. `doi:10.1002/fld.1927`.

[15] T. Belytschko, Y. Guo, W. Kam Liu, S. Ping Xiao, A unified stability analysis of meshless particle methods, Int. J. Numer. Methods Eng. 48 (9) (2000) 1359–1400. `doi:10.1002/1097-0207(20000730)48:9<1359::AID-NME829>3.0.CO;2-U`.

[16] Y. Vidal, J. Bonet, A. Huerta, Stabilized updated lagrangian corrected sph for explicit dynamic problems, Int. J. Numer. Methods Eng. 69 (13) (2007) 2687–2710. `doi:10.1002/nme.1859`.

[17] G. R. Liu, M. B. Liu, Smoothed Particle Hydrodynamics A Meshfree Particle Method, World Scientific Publishing Co Pte Ltd, 2003.

[18] D. J. Price, Magnetic fields in astrophysics, Ph.D. thesis, University of Cambridge (2004).

[19] W. G. Hoover, C. G. Hoover, E. C. Merritt, Smooth-particle applied mechanics: Conservation of angular momentum with tensile stability and velocity averaging, Phys. Rev. E 69 (1) (2004) 016702. `doi:10.1103/PhysRevE.69.016702`.

[20] J. J. Monaghan, On the problem of penetration in particle methods, J. Comput. Phys. 82 (1) (1989) 1–15. `doi:10.1016/0021-9991(89)90032-6`.

[21] W. K. Liu, S. Li, T. Belytschko, Moving least-square reproducing kernel methods (i) methodology and convergence, Comput. Methods Appl. Mech. Eng. 143 (1-2) (1997) 113–154. `doi:10.1016/S0045-7825(96)01132-2`.

[22] S. Li, W. K. Liu, Moving least-square reproducing kernel method part ii: Fourier analysis, Comput. Methods Appl. Mech. Eng. 139 (1-4) (1996) 159–193. `doi:10.1016/S0045-7825(96)01082-1`.

[23] R. Vignjevic, J. C. Campbell, J. Jaric, S. Powell, Derivation of sph equations in a moving referential coordinate system, Comput. Methods Appl. Mech. Eng. 198 (30-32) (2009) 2403–2411. `doi:10.1016/j.cma.2009.02.027`.

[24] J.-l. Lacome, C. Espinosa, J. Limido, Sph formulation with lagrangian eulerian adaptive kernel, in: D. Le Touzé (Ed.), Proc. 4th SPHERIC Work., no. 1, 4th SPHERIC Workshop Local Organization Committee, Nantes, 2009, pp. 294 – 301.

[25] J. R. Young, Modelling elastic dynamics and fracture with coupled mixed correction eulerian total lagrangian sph, Ph.D. thesis, The University of Edinburgh (2018).

[26] J. J. Monaghan, Smoothed particle hydrodynamics, Annu. Rev. Astron. Astrophys. 30 (1) (1992) 543–574. `arXiv:0507472v1, doi:10.1146/annurev.aa.30.090192.002551`.

[27] J. J. Monaghan, Sph and riemann solvers, J. Comput. Phys. 136 (2) (1997) 298–307. `doi:10.1006/jcph.1997.`

5732.

[28] T. De Vuyst, R. Vignjevic, Total lagrangian sph modelling of necking and fracture in electromagnetically driven rings, Int. J. Fract. 180 (1) (2013) 53–70. doi:10.1007/s10704-012-9801-4.

[29] R. Vignjevic, T. De Vuyst, J. C. Campbell, A frictionless contact algorithm for meshless methods, Comput. Model. Eng. Sci. 13 (1) (2006) 35–48.

[30] R. Vignjevic, T. De Vuyst, J. C. Campbell, A frictionless contact algorithm for meshless methods, in: Int. Conf. Comput. Eng. Sci., 2007, pp. 107–112.

[31] J. R. Reveles, Development of a total lagrangian sph code for the simulation of solids under dynamic loading, Ph.D. thesis, Cranfield University (2007).

[32] G. C. Ganzenmüller, An hourglass control algorithm for lagrangian smooth particle hydrodynamics, Comput. Methods Appl. Mech. Eng. 286 (2015) 87–106. doi:10.1016/j.cma.2014.12.005.

[33] B. P. Howell, G. J. Ball, A free-lagrange augmented godunov method for the simulation of elastic–plastic solids, J. Comput. Phys. 175 (1) (2002) 128–167. doi:10.1006/JCPH.2001.6931.

[34] V. Mehra, S. Chaturvedi, High velocity impact of metal sphere on thin metallic plates: A comparative smooth particle hydrodynamics study, J. Comput. Phys. 212 (1) (2006) 318–337. doi:10.1016/J.JCP.2005.06.020.

[35] Z. L. Zhang, M. B. Liu, Smoothed particle hydrodynamics with kernel gradient correction for modeling high velocity impact in two- and three-dimensional spaces, Eng. Anal. Bound. Elem. 83 (2017) 141–157. doi:10.1016/J.ENGANABOUND.2017.07.015.

[36] V. Mehra, C. D. Sijoy, V. Mishra, S. Chaturvedi, Tensile instability and artificial stresses in impact problems in sph, J. Phys. Conf. Ser. 377 (2012) 012102. doi:10.1088/1742-6596/377/1/012102.

[37] H. Asadi Kalameh, A. Karamali, C. Anitescu, T. Rabczuk, High velocity impact of metal sphere on thin metallic plate using smooth particle hydrodynamics (sph) method, Front. Struct. Civ. Eng. 6 (2) (2012) 101–110. doi:10.1007/s11709-012-0160-z.

[38] G. R. Johnson, T. J. Holmquist, Evaluation of cylinderimpact test data for constitutive model constants, J. Appl. Phys. 64 (8) (1988) 3901–3910. doi:10.1063/1.341344.

[39] G. R. Johnson, W. H. Cook, Fracture characteristics of three metals subjected to various strains, strain rates, temperatures and pressures, Eng. Fract. Mech. 21 (1) (1985) 31–48. doi:10.1016/0013-7944(85)90052-9.

[40] L. D. Libersky, A. G. Petschek, T. C. Carney, J. R. Hipp, F. A. Allahdadi, High strain lagrangian hydrodynamics, J. Comput. Phys. 109 (1) (1993) 67–75. doi:10.1006/jcph.1993.1199.

[41] LS-DYNA® Keyword User's Manual, Vol. 2 Material Models, Livermore Software Technology Corporation, 2018.

Author statement

J. Young: Methodology, Software, Investigation, Validation, Formal analysis, Writing - Original draft, Writing - Review & Editing, Visualisation. F. Teixeira-Dias: Formal analysis, Writing - Review & Editing, Resources, Supervision. A. Azevedo: Validation, Formal analysis, Investigation. F. Mill: Supervision, Funding acquisition.

Declaration of interests

The authors declare that they have no known competing financial interests or personal relationships that could have appeared to influence the work reported in this paper.